J. Fluid Mech. (2025), *vol.* 1019, A15, doi:10.1017/jfm.2025.10582

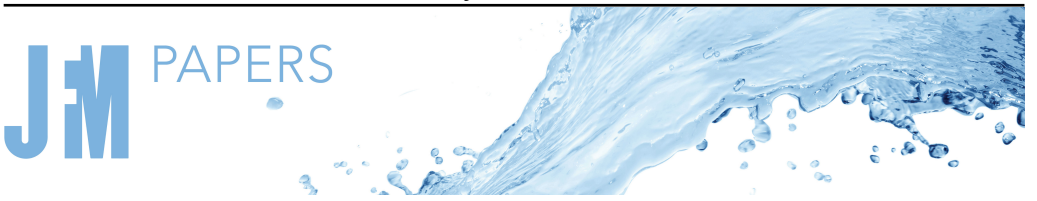

Approach to similarity in the pinch-off of a viscous liquid thread

Marie Corpart[1], **Miguel Ángel Herrada**[2], **Antoine Deblais**[1] and **Daniel Bonn**[1]

[1]Van der Waals-Zeeman Institute, Institute of Physics, University of Amsterdam, Amsterdam 1098XH, Netherlands

[2]Depto. de Mecánica de Fluidos e Ingeniería Aeroespacial, Universidad de Sevilla, Sevilla E-41092, Spain

Corresponding author: Marie Corpart, m.corpart@uva.nl

(Received 20 December 2024; revised 21 May 2025; accepted 5 August 2025)

The breakup of viscous liquid threads is governed by a complex interplay of inertial, viscous and capillary stresses. Theoretical predictions near the point of breakup suggest the emergence of a finite-time singularity, leading to universal power laws describing the breakup, characterised by a universal prefactor. Recent stability analyses indicate that, due to the presence of complex eigenvalues, achieving similarity may only be possible through time-damped oscillations, making it unclear when and how self-similar regimes are reached for both visco-inertial and viscous regimes. In this paper, we combine experiments with unprecedented spatio-temporal resolution and highly resolved numerical simulations to investigate the evolution of the liquid free surface during the pinching of a viscous capillary bridge. We experimentally show for the first time that, for viscous fluids the approach to the self-similar solution is composed of a large overshoot of the instantaneous shrinking speed before the system converges to the nonlinear pinch-off similarity solution. In the visco-inertial case, the convergence to the stable solution is oscillatory, whereas in the viscous case, the approach to singularity is monotonic. While our experimental and numerical results are in good agreement in the viscous regime, systematic differences emerge in the visco-inertial regime, potentially because of effects such as polymer polydispersity, which are not incorporated into our numerical model.

Key words: drops and bubbles, interfacial flows (free surface)

1. Introduction

Liquid thread breakup is a phenomenon of paramount importance in various scientific and industrial contexts (Eggers 1997; Eggers & Villermaux 2008), ranging from dripping

faucets (Ambravaneswaran *et al.* 2000, 2004) to the design of microfluidic devices (Stone, Stroock & Ajdari 2004) or inkjet printing applications such as electronic circuits (Sirringhaus *et al.* 2000; Caironi *et al.* 2010) and living cells (Xu *et al.* 2005; Calvert 2007).

For the case of Newtonian fluids, the thread undergoes a spontaneous capillary-driven thinning, while the dynamics is slowed down by the interplay of viscous and inertial stresses. The dynamics of this pinch-off process exhibits a finite-time singularity, where, for an axisymmetric system, the minimal radius of the liquid thread $R_{min}(z, t)$ (with z the direction of gravity and t the time) is exactly equal to zero at a finite time for $z = z_c$ and $t = t_c$. The mathematical analysis close to this singularity suggests the emergence of various self-similar regimes depending on the competition of the forces at play (Eggers 1997; Eggers & Villermaux 2008). They are characterised by the self-similarity of the neck profiles

$$\frac{R(z,t)}{R_{min}(t)} = \frac{\phi(\xi)}{\mathcal{A}}, \tag{1.1}$$

where ϕ is a self-similar function, $\mathcal{A}$ a constant and ξ the self-similar variable defined as $\xi = l'/|t'|^{\beta}$, with $l' = (z - z_c)/\ell_\eta$ and $t' = (t_c - t)/\tau_\eta$. Here, ϕ and $\mathcal{A}$ are used as general notations to denote the self-similar function and numerical prefactor resulting from the self-similar analysis of the long-wave jet equations in either the inertial, visco-inertial or viscous regimes. The intrinsic length and time scales of the system are $\ell_\eta = \eta^2/(\rho\gamma)$ and $\tau_\eta = \eta^3/(\rho\gamma^2)$, where η is the viscosity, γ is the surface tension and ρ is the density of the fluid. In the self-similar regime, the minimum of the neck radius then thins as a power law of the time to pinch-off $t_c - t$

$$\frac{R_{min}(t)}{R_0} = \mathcal{A}\left(\frac{t_c - t}{\tau^\star}\right)^{\alpha}, \tag{1.2}$$

with $\tau^\star$ a characteristic time scale of the system and α the power-law exponent, which takes a value of 2/3 in the case of negligible viscosity, and 1 otherwise.

For viscous fluids, thinning is governed by the competition between viscosity and capillarity (Papageorgiou 1995; Eggers 1995), where the minimum neck radius evolves as described in 1.2 with a prefactor $\mathcal{A}_V = 0.07$ and with $\tau^\star = t_v = \eta R_0/\gamma$ the visco-capillary time. In this limit, the self-similar function ϕ is symmetrical and $\beta \approx 0.175$ (Papageorgiou 1995; Eggers 1995). This means that the thread profiles, in the parameter space R/R_{min} vs ξ, are expected to be symmetric around z_c when approaching breakup. As the singularity is approached, the deformation rate in the fluid continues to increase until inertia becomes significant and can no longer be neglected. Eventually, a balance between surface tension, viscosity and inertia is reached, resulting in the universal visco-inertial regime of Eggers for which the prefactor is $\mathcal{A}_{IV} = 0.03$. In this case, the self-similar function ϕ is asymmetrical, and $\beta = 0.5$ (Eggers 1993).

Self-similar regimes have been reported in both experiments (Kowalewski 1996; Chen & Steen 1997; Cohen *et al.* 1999; Cohen & Nagel 2001; Rothert *et al.* 2001; Chen, Notz & Basaran 2002) and numerics (Chen & Steen 1997; Day, Hinch & Lister 1998; Zhang & Lister 1999; Chen *et al.* 2002; Sierou & Lister 2003). They are often used as a powerful tool, for instance, to determine the dynamical properties of liquids (Roché *et al.* 2009; de Saint Vincent *et al.* 2012). However, to obtain reliable results from this method, it is necessary either to ensure that the system has converged to the self-similar solution or at least to know the temporal evolution of the slope of $(R_{min}/R_0)^{1/\alpha}$ which should be a constant equal to the prefactor $\mathcal{A}$, provided that the system has converged to the similarity solution. Recent results have shown that convergence can be slow because the system may exhibit transient regimes, multiple transitions or oscillations between regimes

(Doshi *et al.* 2003; Castrejón-Pita *et al.* 2015; Li & Sprittles 2016; Lagarde, Josserand & Protière 2018; Deblais *et al.* 2018; Rubio *et al.* 2019). For inviscid fluids slowly dripping from a nozzle, convergence to the inertial self-similar solution is not observed (Deblais *et al.* 2018). All this makes it unclear when and how the prefactor should converge toward its expected asymptotic value. Besides the fundamental importance of this issue, this has led to incorrect measurements of the physico-chemical properties of the fluids involved (Hauner *et al.* 2017).

In this article, we aim to clarify the conditions under which similarity solutions emerge for viscous pinching. To this end, we conducted experiments with unprecedented spatio-temporal resolution, combined with high-resolution numerical simulations, to study the evolution of a viscous liquid thread (silicone oils) until its breakup. Our findings reveal that, for viscous liquids, the approach to similarity is non-monotonic prior to convergence to the viscous similarity solution before inertia enters the picture. In contrast, for lower-viscosity liquids, the self-similar visco-inertial regime is reached through a transient oscillatory regime, which arises from the presence of complex eigenvalues recently evidenced in a theoretical paper (Dallaston *et al.* 2021). Interestingly, in the visco-inertial regime, we observe that the convergence occurs earlier in the experiments than in the numerical simulations. This systematic discrepancy suggests that physical effects not accounted for in our numerical model, such as finite-size effects or a gradient in chain length distribution due to polymer polydispersity, may influence the late-stage dynamics. These findings highlight the need for further investigation into the microstructural properties of the fluid when comparing experimental data with theoretical predictions.

2. Experimental methods

To study the thinning and pinch-off of viscous filaments, we performed experiments using silicone oils (Polydimethylsiloxane (PDMS), Sigma-Aldrich) with a density of $\rho = 970\,\mathrm{kg\,m^{-3}}$, surface tension of $\gamma = 20\,\mathrm{mN\,m^{-1}}$ and three different viscosities: $\eta = 100$, 500 and $1000\,\mathrm{mPa\cdot s}$. We used a custom-built capillary breakup extensional rheometry set-up, similar to the set-up described by Gaillard *et al.* (2024), where a drop is initially placed on a horizontal plate of radius $R_0 = 1$, 1.75 or 2.5 mm. Initially, the motor-driven top plate of the same radius is lowered until it makes contact with the bottom plate. Subsequently, the top plate is slowly raised until a stable capillary bridge is formed at an initial separation distance L_0. The top plate is then incrementally raised in steps of $10\,\mu\mathrm{m}$, with a wait time of approximately 10 s between each step to ensure bridge stability. Ultimately, the bridge becomes unstable and pinches at a certain distance between the plates due to capillary forces. The entire set-up is mounted on an optical table to minimise external disturbances during the breakup process.

The thinning of the bridge is captured using a high-speed camera (Phantom TMX 7510, Vision Research) equipped with a long working distance microscope objective offering 20x magnification (Edmund Optics, 20X M Plan Apo, WD = 20 mm, Infinity Corrected). Pinch-off events are recorded at speeds of up to 110 000 frames per second with a spatial resolution of $1.1\,\mu\mathrm{m\,pixel^{-1}}$. A typical thread breakup is shown in the top panel of figure 1. Image analysis is performed using a custom Python code that detects the liquid/air interfaces by applying Sobel filtering to the images. Subsequently, it allows us to extract the neck profile $R(z, t)$ and the minimum neck radius $R_{min}(t)$ (see figure 5 for more details on the procedure). From the image analysis, we determined that it is possible to accurately measure the minimum diameter of the neck down to 3 pixels. This corresponds to a physical size of $R_{min} \approx 1.6\,\mu\mathrm{m}$.

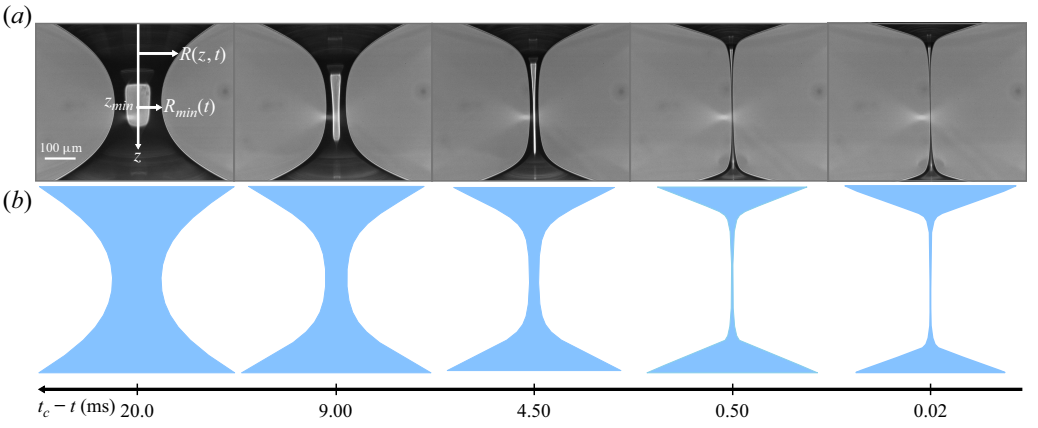

Figure 1. High-speed image sequence (*a*) and numerical simulations (*b*) of the thinning of a viscous thread; the liquid shown here is PDMS with viscosity $\eta = 500$ mPa · s initially placed between two plates of diameter $R_0 = 1$ mm; simulations show two-dimensional cuts through the z-axis. The time to pinch-off ($t_c - t$) is indicated at the bottom of the figure.

The time of pinch-off t_c is determined as the time between the last frame in which the filament remains attached and the first frame where the filament breaks. The typical error in the determination of t_c is therefore of the order of 20 µs.

We define an effective deformation rate as $\dot{\epsilon} = 1/R_{min}(\mathrm{d}R_{min}/\mathrm{d}t)$. From our experimental data, we obtain that the deformation rate increases as the filament thins and that the maximum deformation rate is $\dot{\epsilon} \sim 10^3\ \mathrm{s}^{-1}$. For this magnitude of shear rate, usually reached in routine rheological controlled shear-rate measurements, the silicone oils we used for our experiments do not show non-Newtonian behaviour.

3. Numerical methods

We simulated the pinch-off dynamics of high-viscosity capillary bridges using a modified version of the method introduced by Herrada & Montanero (2016), previously applied to fluids of low to intermediate viscosity (Deblais *et al.* 2018; Rubio *et al.* 2019). The method relies on a quasi-elliptic analytical mapping that transforms the original, time-evolving physical domain into a fixed rectangular computational domain, $[0 \leqslant s \leqslant 1] \times [0 \leqslant \eta \leqslant 1]$. This facilitates the application of efficient numerical schemes while preserving accuracy near the singularity.

In the transformed domain, the governing equations are discretised using n_η Chebyshev spectral collocation points in the η-direction and second-order finite differences with n_s uniformly spaced points in the s-direction. For the simulations reported here, we used $n_s = 5001$ and $n_\eta = 10$. Time integration is performed with a second-order backward differentiation scheme and adaptive time stepping, ensuring stable and accurate evolution up to $R_{min}/R_0 \sim 10^{-5}$ (i.e. $R_{min} \sim 0.1$ µm). The pinch-off time t_c is estimated by linearly extrapolating the final numerical data, justified by the self-similar linearity near singularity.

Mesh convergence was verified for $\eta = 100$ mPa · s using three resolutions: 4001×9, 5001×10, and 6001×11. As shown in figure 6(*a*,*b*), the results are insensitive to mesh size. For further validation, simulations were also conducted using the Basilisk code (http://basilisk.fr/). As shown in figure 6(*c*,*d*), both codes agree up to $R_{min}/R_0 = 10^{-3}$, although Basilisk fails closer to pinch-off due to numerical instability, while the

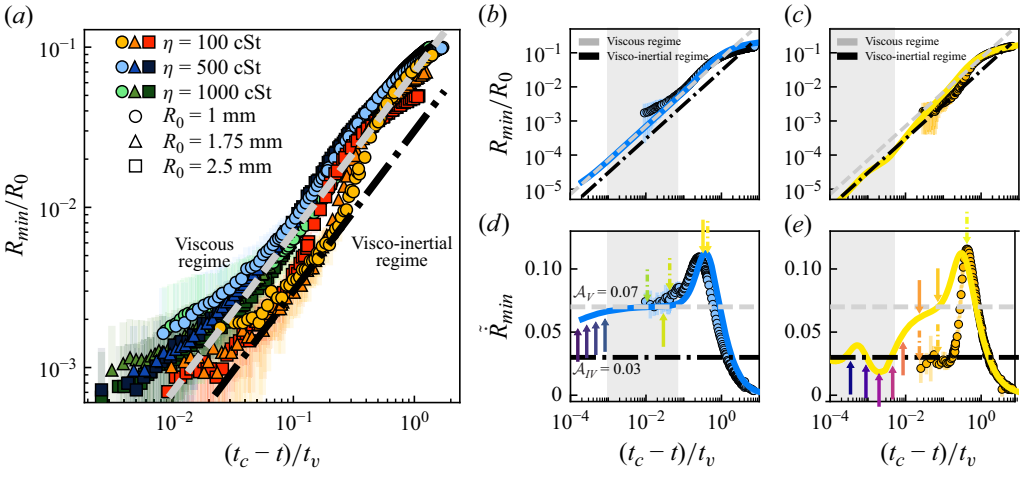

Figure 2. Minimum neck radius and shrinking speed versus time. (*a*) Experimental dimensionless neck radius R_{min}/R_0 versus viscous-scaled time to pinch-off $(t_c - t)/t_v$ for silicone oils with different viscosities η and plate radii R_0. (*b–e*) Experimental (◯) and numerical (solid lines) results for $R_0 = 1$ mm, $Bo = 0.45$. (*b*,*c*) Dimensionless neck radius R_{min}/R_0 and (*d*,*e*) dimensionless shrinking speed $\tilde{\dot{R}}_{min} = -\dot{R}_{min}\eta/\gamma$ as functions of $(t_c - t)/t_v$ for $\eta = 500$ mPa · s ($Oh = 3.5$; *b*,*d*) and $\eta = 100$ mPa · s ($Oh = 0.7$; *c*,*e*). Grey shaded regions mark the time intervals where the shrinking speed approaches the theoretical prefactor $\mathcal{A}$. Grey dashed lines: viscous regime. Black dash-dotted lines: visco-inertial regime. Arrows indicate shrinking speeds corresponding to the profiles in figure 4: full arrows for numerics (figure 4*a*,*b*), dashed for experiments (figure 4*c*,*d*).

Jacobian Analytical Method (JAM) solver (https://miguelherrada.github.io/JAM/) reaches $R_{min}/R_0 = 10^{-5}$. At $R_{min}/R_0 = 10^{-3}$, both codes produce identical profiles (figure 6*d*), confirming consistency.

We also compared our numerical results with those of Li & Sprittles (2016), who studied an identical geometry. As shown in figure 7, the agreement between the two studies confirms the robustness and accuracy of our numerical approach.

To match the numerics with the experiments, the volume of liquid used in the numerical simulations is adjusted to ensure that the length of the liquid bridge is the same as that observed in the experiments. This corresponds to a volume of 2 µl for $\eta = 500$ mPa · s and 0.8 µl for $\eta = 100$ mPa · s. Figures 1(*b*) and 8 show the numerical profiles at various times before pinch-off.

4. Results and discussion

The time evolution of the experimentally measured minimum neck radius for all tested conditions is presented in figures 2(*a*) and 3(*a–c*). In the slow deformation limit, the dimensionless numbers governing the thinning dynamics are the Ohnesorge number $Oh = \eta/(\sqrt{\rho R_0 \gamma})$ and the Bond number $\mathrm{Bo} = \rho g R_0^2/\gamma$, where g is the gravitational acceleration. For highly viscous liquids with $\eta = 500$ and $\eta = 1000$ mPa · s, corresponding to $Oh \in [2, 7]$, all data points align on a curve that follows, within the error bars, the prediction for the viscous regime, highlighted by the dashed grey line. In contrast, for an intermediate viscosity of $\eta = 100$ mPa · s, corresponding to $Oh \in [0.4, 0.7]$, an apparent transition between the viscous and visco-inertial regimes is observed, seemingly dependent on R_0. Near the point of pinch-off, the results fall onto the same master curve, consistent with the visco-inertial regime (dashed black line). To follow the eventual convergence towards the similarity solution, we calculated instantaneous values of the dimensionless shrinking speed $\tilde{\dot{R}}_{min} = -\dot{R}_{min}\eta/\gamma$ from the local slope of the dynamics,

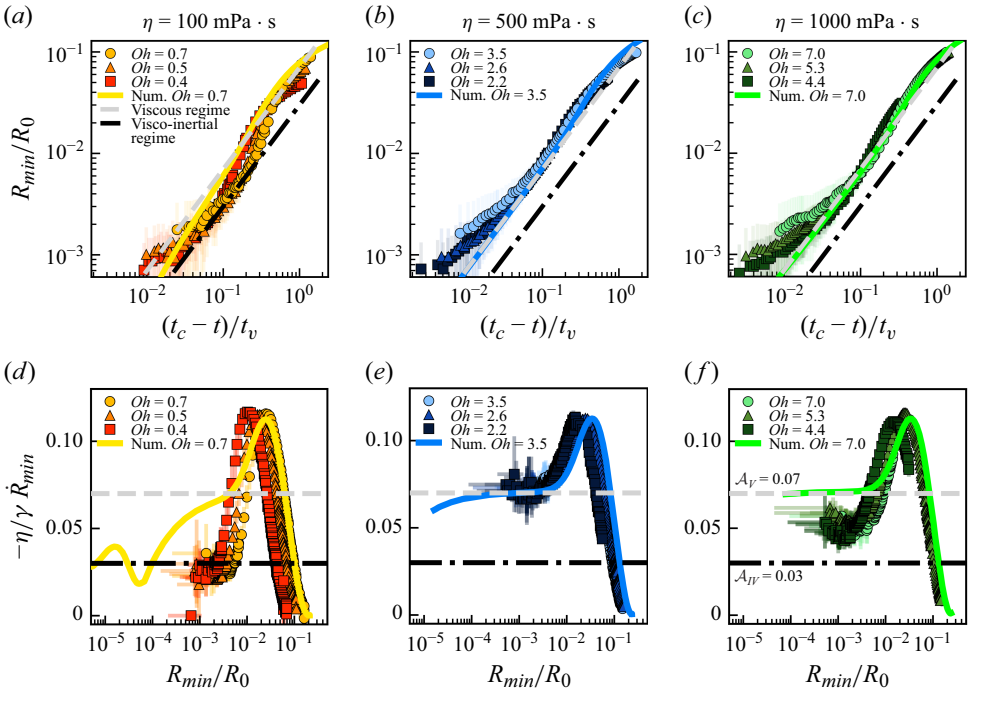

Figure 3. Influence of R_0 on neck dynamics across viscosities. Top row: dimensionless neck radius R_{min}/R_0 versus dimensionless time $(t_c - t)/t_v$. Bottom row: dimensionless shrinking speed $-\dot{R}_{min}\eta/\gamma$ versus R_{min}/R_0. Data are shown for all tested R_0 and for each fluid viscosity. Viscosity values: (*a*,*d*) $\eta = 100$ mPa · s, (*b*,*e*) $\eta = 500$ mPa · s, (*c*,*f*) $\eta = 1000$ mPa · s.

which should be equal to the value of the prefactor $\mathcal{A}$ if the system has converged to the similar solution (see (1.2)).

Figures 2(*d*,*e*) and 3(*c*–*e*) show respectively the evolution of $\tilde{\dot{R}}_{min}$ as a function of the dimensionless breakup time $(t_c - t)/t_v$ and of the dimensionless neck radius R_{min}/R_0. Comparing figures 2(*d*,*e*) and 3(*d*,*e*) shows that representing the evolution of $\tilde{\dot{R}}_{min}$ as a function of $(t_c - t)/t_v$ or of R_{min}/R_0 is interchangeable, demonstrating the reliability of our determination of t_c. All datasets exhibit a non-monotonic variation of $\tilde{\dot{R}}_{min}$, reaching a maximum before it drops and eventually converges to the expected asymptotic value, either $\mathcal{A}_V = 0.07$ for the viscous regime or $\mathcal{A}_{IV} = 0.03$ for the visco-inertial regime. The initial overshoot in shrinking speed marks the transition from the exponentially growing Rayleigh instability to the nonlinear similarity solution. Figures 2(*d*,*e*) and 3(*d*,*e*) show the evolution of $\tilde{\dot{R}}_{min}$ for the two different regimes: the initial overshoot is nearly identical when plotted against the dimensionless viscous time. In the following, we discuss in more details the convergence toward each self-similar regime.

4.1. *Viscous regime*

We start by examining the results for viscous liquids (figures 2*b*,*d* and 3*b*,*c*,*e*,*f*).

In this regime, for $\eta = 500$ mPa · s, the agreement between experiments and simulations remains robust across a range of conditions. Notably, the plate radius R_0, and thus the Ohnesorge number, has no influence on the temporal evolution (figure 3*b*,*e*). However, at higher viscosities (figure 3*c*,*f*), discrepancies between experiment and simulation appear.

These deviations arise from increasing experimental noise: as viscosity increases, the thinning rate $\mathrm{d}R_{min}/\mathrm{d}t$ becomes smaller, making accurate measurement more challenging. This results in a systematic underestimation of the instantaneous shrinking speed. The effect is clearly visible in figure 9, which presents raw data from multiple independent experiments with different initial droplet radii. The scatter increases markedly at $\eta = 1000$ and 10 000 mPa · s. Consequently, average values derived from these measurements (figure 3*f*) exhibit a downward bias due to these limitations.

For this reason, we focus on the case $Oh = 3.5$ shown in figure 2(*b*,*d*) for which the parameters match those used in our numerical simulations. After the overshoot in the instantaneous shrinking speed, $\tilde{\dot{R}}_{min}$ converges toward the asymptotic value $\mathcal{A}_V = 0.07$, consistent with the criterion proposed by Li and Sprittles (Li & Sprittles 2016), which predicts the transition when $R_{min}/R_0 \approx 10^{-2}$ (figure 7). At this stage, the thread is sufficiently slender to validate the assumptions underlying the viscous similarity solution (Li & Sprittles 2016). The monotonic convergence toward $\mathcal{A}_V$ further confirms the stability of this regime, in line with the eigenvalue analysis of Eggers (Eggers 2012).

To examine the regime closer to pinch-off, we rely on numerical simulations as the optical resolution of our experiments limits our access to very small time scales. We observe that $\tilde{\dot{R}}_{min}$ begins to deviate downward from the asymptotic value, which we attribute to the onset of inertial effects. To isolate their contribution, we performed simulations both without inertia (by setting $\rho = 0$) and without gravity (see the solid pink and dashed blue lines in figure 10(*a*), respectively). Without inertia, the shrinking speed remains constant at $\mathcal{A}_V = 0.07$, while the influence of gravity is negligible. Once again, the criterion of Li and Sprittles (Li & Sprittles 2016), $R_{min}/R_0 \approx 5.5 \times 10^{-4}\, Oh^{-3.1} \approx 10^{-5}$, accurately predicts the onset of inertial deviation (figure 7).

Further insight comes from analysing the neck profiles over time. Figure 4(*a*,*c*) displays experimental and numerical profiles at various times prior to pinch-off for the same viscous fluid. The corresponding times are marked in figure 2(*d*). As $\tilde{\dot{R}}_{min}$ approaches $\mathcal{A}_V$, the profiles become symmetric and self-similar, and can be collapsed onto one another using the viscous similarity variable ξ. The agreement with the theoretical self-similar profile (grey dashed lines) is excellent. However, near pinch-off, the numerical profiles deviate from this U-shaped form due to inertial effects. This deviation is absent in inertia-free simulations (see figure 11*f*).

Altogether, these observations confirm that, for $Oh \gg 1$, the system converges to the self-similar viscous regime both in simulations and experiments once $R_{min}/R_0 \leqslant 10^{-2}$. For the case studied here (figure 2*b*,*d*), this convergence occurs within a few milliseconds of the pinch-off event.

4.2. *Visco-inertial regime*

We now turn to less viscous fluids ($\eta = 100$ mPa · s), for which we observe a more complex behaviour. Figures 2(*c*) and 3(*d*) show a similar non-monotonic variation of $\tilde{\dot{R}}_{min}$ as observed in the viscous case, with a rather large overshoot before decreasing towards the asymptotic visco-inertial value $\mathcal{A}_{IV} = 0.03$. In contrast to the viscous regime, a dependence on R_0 in the convergence to the visco-inertial regime is observed (figure 3*a*,*d*), consistent with the predictions of Li & Sprittles (2016) (see figure 7). Interestingly, while Li and Sprittles report that the velocity curves shift toward smaller times (i.e. to the right in figure 3*d*) with increasing Ohnesorge number, our experimental data show a shift in the opposite direction. At present, the origin of this discrepancy remains unclear, and this observation warrants further investigation.

We now focus on the case $Oh = 0.7$, shown in figure 2(*c*,*e*), for which the parameters match those used in our numerical simulations. The numerical results for $\tilde{\dot{R}}_{min}$ align well with those obtained by Li and Sprittles (Li & Sprittles 2016) regarding the transition into the viscous regime ($R_{min}/R_0 \approx 10^{-2}$), the exit from the viscous regime ($R_{min}/R_0 \approx 5.5 \times 10^{-4} Oh^{-3.1}$) and the transition into the visco-inertial regime ($R_{min}/R_0 \approx 2.3 \times 10^{-4} Oh^{-3.1}$).

However, discrepancies emerge when comparing experiments and simulations. In particular, the convergence of $\tilde{\dot{R}}_{min}$ to the visco-inertial asymptotic value $\mathcal{A}_{IV}$ occurs earlier in the experiments than in the numerical simulations. To investigate this, we introduced thermal noise into the numerical model, since noise has previously been shown to influence the pinch-off dynamics (Shi, Brenner & Nagel 1994). However, this modification did not reproduce the experimental observations. We hypothesise that the earlier convergence may originate from the polydispersity of PDMS chain lengths. Specifically, a viscosity gradient along the filament, caused by a higher concentration of short chains near the neck, could accelerate the transition to the visco-inertial regime. Such effects of polydispersity have been reported before; for instance, Champougny *et al.* (2017) showed that even small surface tension gradients due to polydispersity can overstabilise free films withdrawn from a PDMS bath. To test this hypothesis, future experiments should be conducted using monodisperse PDMS.

Finally, for times very close to pinch-off, the instantaneous shrinking speed exhibits oscillations before eventually converging. The oscillatory convergence of $\tilde{\dot{R}}_{min}$ to $\mathcal{A}_{IV}$ is apparent in the experimental data (figure 2*e*), although uncertainties near the singularity limit definitive conclusions. The oscillatory behaviour observed in low-viscosity fluids can be attributed to the presence of complex eigenvalues in the stability analysis of the visco-inertial similarity solution. Dallaston *et al.* (2021) predict that one full oscillation occurs as $t_c - t$ decreases by a factor of approximately 16. This agrees well with our simulations, which show a complete oscillation over the same interval (figure 2*e*). Furthermore, in the first half-oscillation, $t_c - t$ decreases by a factor of approximately 5 in the simulations, which is consistent with the experimental decrease of approximately a factor of 4. These comparisons further validate the consistency of our experimental and numerical approaches.

Figure 4(*b*,*d*) shows the numerical and experimental neck profiles at different times before pinch-off for the same low-viscosity fluid. The corresponding times are indicated by solid (numerical) and dashed (experimental) arrows in figure 2(*e*). As the singularity is approached, the profiles transition from symmetric to asymmetric, as expected in the visco-inertial regime (Eggers 1993). Interestingly, both numerical and experimental profiles remain symmetric for a short interval even after $\tilde{\dot{R}}_{min}$ has reached $\mathcal{A}_{IV}$. In the simulations, the profiles exhibit oscillations around the asymmetric visco-inertial self-similar solution, shown as black dashed lines in figure 4(*b*,*d*) (see also figure 11 for gravity-free profiles).

The oscillatory behaviour observed in low-viscosity fluids explains the difficulty in experimentally capturing clean visco-inertial similarity solutions, as also noted by Deblais *et al.* (2018) for inertial fluids. Figure 4(*d*) suggests that, while the experimental profiles are close to self-similar, they do not converge to the expected asymmetric shape (Eggers 1993). This highlights a key difference: whereas simulations display oscillatory convergence to the visco-inertial regime, the experimental data do not provide definitive evidence of such convergence. These results emphasise the practical difficulty of achieving visco-inertial self-similarity in low-viscosity fluids.

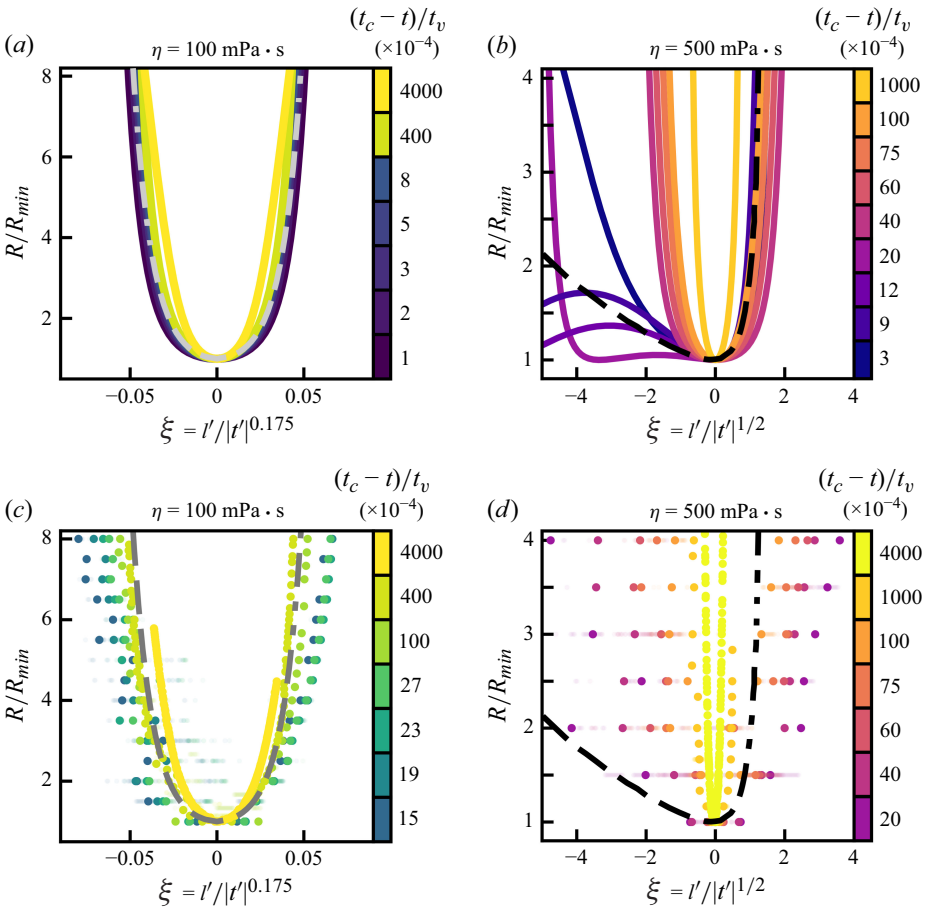

Figure 4. Dimensionless profiles of the neck $R(z, t)/R_{min}$ as a function of the self-similar variable ξ for different values of the dimensionless time to pinch-off. The left column shows the results for $\eta = 500$ mPa · s ($Oh = 3.5$) and the right column the results for $\eta = 100$ mPa · s ($Oh = 0.7$), in all cases $R_0 = 1$ mm (Bo = 0.45). (*a*,*b*) Numerical profiles and (*c*,*d*) experimental profiles. The dimensionless times to pinch-off corresponding to the profiles are indicated on figure 2(*d*,*e*) by the solid (numerical simulations) and dashed (experiments) arrows. The lighter coloured dots show the typical error in determining the neck profiles in the experiments. The black dashed lines show the universal visco-inertial self-similar solution adapted from Eggers (1993). The grey dashed lines represent the viscous self-similar solution obtained from equation (158) of Eggers (1997) with a normalisation length $\bar{\xi} = 160$.

Moreover, a satellite droplet forms between the two pinch-off points in the simulations (see figure 12). This feature is characteristic of the visco-inertial regime. However, it is not observed experimentally, likely because it falls below the optical resolution. Consistent with this explanation, numerical profiles suggest that its radius is of the order of 100 nm.

4.3. *Discussion*

Our results clearly demonstrate a distinction between two behaviours. First, all tested fluids exhibit a large overshoot of $\tilde{R}_{min}$, regardless of Ohnesorge number, a signature of the transition from the Rayleigh instability to a nonlinear similarity regime. Then, for highly viscous fluids ($Oh \gg 1$), the convergence to the viscous similarity solution is monotonic.

For less viscous fluids ($Oh \lesssim 1$), the convergence to the visco-inertial similarity solution is oscillatory in the numerics, and likely oscillatory in the experiments as well. These distinct behaviours are consistent with the stability analyses of Eggers (2012) and Dallaston *et al.* (2021), which predict a change in the nature of the eigenvalues at $Oh \approx 1$. Furthermore, our findings indicate that the instantaneous shrinking speed exhibits a delayed convergence in both regimes, underscoring the need for careful experimental design when using similarity solutions to infer fluid rheological properties (Hauner *et al.* 2017).

5. Conclusion

In this study, we have investigated both experimentally and numerically the approach to self-similarity in viscous thread breakup. Our key findings are the following. For fluids of non-negligible viscosity ($Oh \sim 1$ or $Oh \gg 1$), we observe a non-monotonic approach to the similarity solution characterised by a large overshoot of the dimensionless instantaneous shrinking speed $\tilde{\dot{R}}_{min}$ when the system transitions between the Rayleigh instability and the pinch-off similarity solution.

For highly viscous fluids ($Oh \gg 1$), we observe that the dimensionless instantaneous shrinking speed converges monotonically to the expected viscous value of $\mathcal{A}_V = 0.07$. Our numerical simulations align closely with the experimental observations. Upon convergence of $\tilde{\dot{R}}_{min}$, the neck profile profile corresponds to the symmetric self-similar solution characteristic of the viscous regime, as described by Papageorgiou and Eggers (Papageorgiou 1995; Eggers & Villermaux 2008). We establish that the self-similar regime is attained for viscous pinch-off when R_{min}/R_0 falls within the range of 10^{-2} to $5.5 \times 10^{-4} Oh^{-3.1}$, consistent with the findings of Li and Sprittles (Li & Sprittles 2016).

For less viscous fluids ($Oh \lesssim 1$), we observe for the first time the oscillatory approach to the visco-inertial similarity solution, with the instantaneous speed $\tilde{\dot{R}}_{min}$ exhibiting damped oscillations before converging to $\mathcal{A}_{IV} = 0.03$. We also observe an earlier convergence of $\tilde{\dot{R}}_{min}$ towards Eggers' value in experiments compared with numerical simulations. Despite this discrepancy, both numerical and experimental profiles initially exhibit symmetry even after $\tilde{\dot{R}}_{min}$ has converged to $\mathcal{A}_{IV} = 0.03$. Within the limit of our numerical and experimental resolutions, these profiles deviate from the self-similar solution expected in the visco-inertial regime, as proposed by Eggers (Eggers 1993). These results suggest that achieving the self-similar regime in the visco-inertial regime remains challenging when studying the pinch-off of a capillary bridge between two pillars in air. We confirm the existence of a transition between these two behaviours at $Oh \approx 1$, as predicted by theoretical stability analyses.

Our high-resolution experiments and simulations reveal the importance of inertial effects in the final stages of breakup, even for highly viscous fluids. These results provide crucial insights into the dynamics of viscous thread breakup and resolve long-standing questions about the approach to self-similarity in different viscosity regimes. Before reaching the universal regime, the system undergoes a non-monotonic transient phase, followed by either monotonic or oscillatory convergence to self-similarity. This behaviour complicates the direct application of asymptotic expressions and universal prefactors in practical contexts. This has important implications for various applications, including inkjet printing, microfluidics and the measurement of fluid properties through capillary breakup experiments.

Future work could explore the influence of non-Newtonian rheology on the self-similar dynamics. Another important direction would be to investigate lower Ohnesorge number regimes ($Oh < 0.15$) to further characterise the low Ohnesorge viscous regime

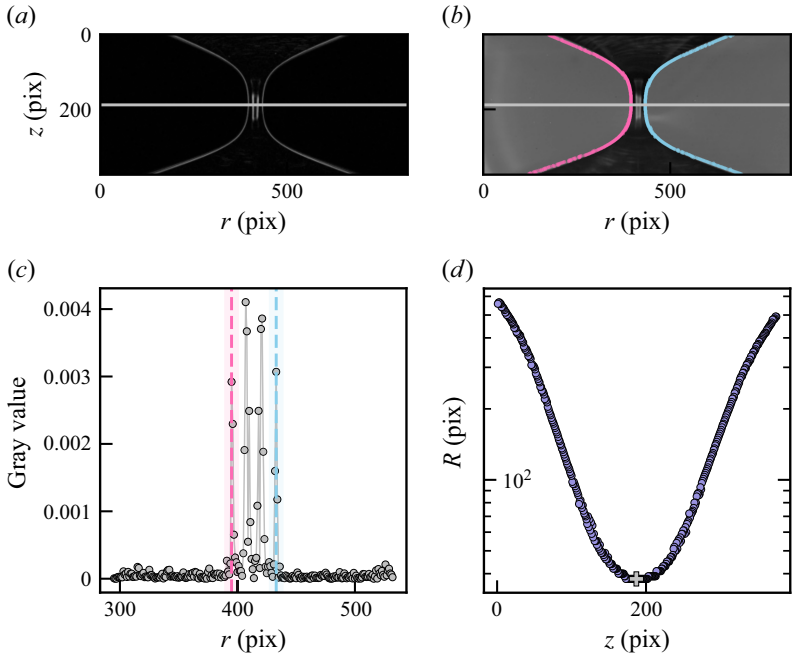

Figure 5. Image processing methods. (*a*) Sobel filtered image and (*b*) raw image of a PDMS bridge during pinching ($R_0 = 2.5$ mm and $\eta = 100$ mPa · s). The grey lines show the detected position of the minimum. (*c*) Grey values on the Sobel filtered image (*a*) along the grey line shown on (*a*) and detection of the left (pink) and right (blue) interface. The detected interfaces are shown with the same colour code in (*b*). (*d*) Spatial evolution of the neck radius $R(z)$ measured on the image. The grey plus shows the coordinates (z_{min}, R_{min}) of the minimum.

(Castrejón-Pita *et al.* 2015; Li & Sprittles 2016). New experiments using monodisperse PDMS could also help to test our hypothesis regarding the discrepancies between numerical and experimental results for low viscous fluids ($Oh = 0.7$, $\eta = 100$ mPa · s). In addition, the use of techniques such as rapid plate retraction in capillary bridge breakup or drop dripping would allow the slender regime to be reached earlier, i.e. at larger R_{min}, thus facilitating more accurate measurements. Extending this analysis to other geometries, such as dripping or jetting configurations, may provide further insight into the universality of these phenomena.

Acknowledgements. We are very grateful to the technology centre of the university of Amsterdam for technical assistance with the set-up. The authors would like to thank S. Popinet and J.M. López-Herrera for their help with the Basilisk simulations.

Funding. M.A.H. acknowledges funding from the Spanish Ministry of Economy, Industry and Competitiveness under grant no. PID2022-14095OB-C21.

Declaration of interests. The authors report no conflict of interest.

Author contributions. M.C. conceived the experiment, obtained and processed the experimental data. M.A.H. obtained the simulation results. All the authors discussed the experimental and numerical results and contributed to the final version of the manuscript.

Appendix A. Image processing method

The image processing method is summarised in figure 5. The images are Sobel filtered to detect the edges of the capillary bridge. Then the background is subtracted from the image

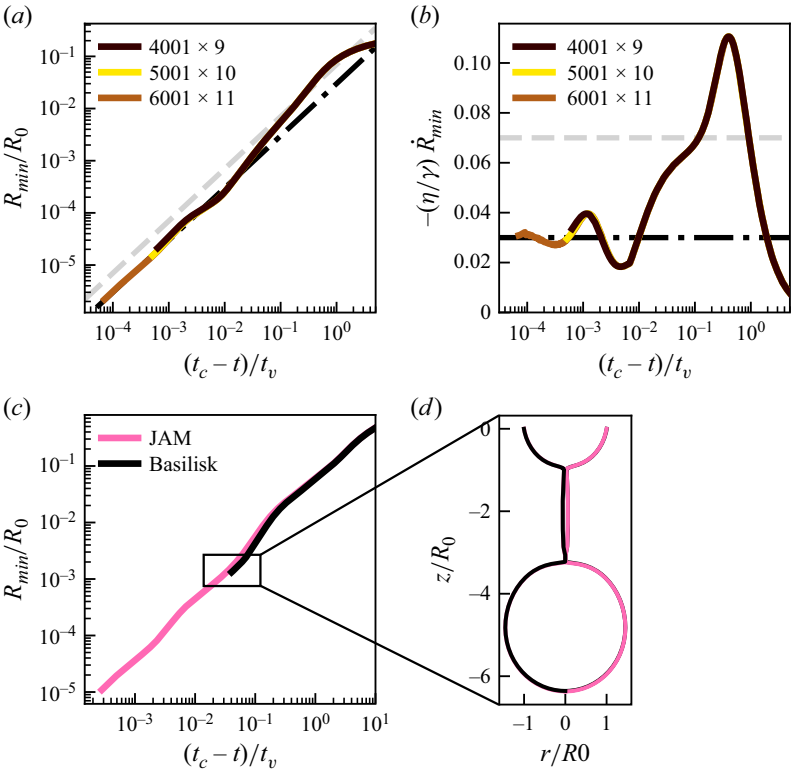

Figure 6. Numerical method. (*a*,*b*) Effect of mesh size on time evolution of neck radius (*a*) and instantaneous velocity (*b*) for $\eta = 100$ mPa · s, $R_0 = 1$ mm, $Oh = 0.7$. The mesh size used for each numerical simulation is given in the legend. The data plotted in figure 2(*c*,*d*) of the main article are shown in yellow. (*c*,*d*) Comparison between JAM and Basilisk for a drop dripping from a needle for $R_0 = 1$ mm and $Oh = 0.16$. (*c*) Temporal evolution of the neck radius and (*d*) profiles of the drop corresponding to $R_{min}/R_0 = 1 \times 10^{-3}$ smallest size resolved with Basilisk.

using the last image (no capillary bridge) as the background. The left and right liquid interfaces are then located on the Sobel image (figure 5*a*) by detecting the first left and right peaks in intensity along each line of the image (figure 5*c*). The detected interfaces are plotted on the raw image in figure 5(*b*) to show the good agreement between the detected interfaces and the image. The spatial evolution of the neck profile $R(z)$ is then calculated as (right − left)/2 (figure 5*d*). The minimum R_{min} and its position z_{min} are then obtained from $R(z)$ (see grey plus in figure 5*d*). With this method we could measure $2R_{min}$ down to 3 pixels which corresponds to a minimum physical size of approximately 1.6 μm

Appendix B. Validation of the numerical method

Mesh convergence was verified for $\eta = 100$ mPa · s using three different spatial resolutions: 4001 × 9, 5001 × 10 and 6001 × 11. As shown in figure 6(*a*,*b*), the results are independent of mesh size, confirming numerical convergence. For further validation, additional simulations were performed using the Basilisk code (http://basilisk.fr/). As illustrated in figure 6(*c*,*d*), both Basilisk and JAM (https://miguelherrada.github.io/JAM/) yield identical results down to $R_{min}/R_0 = 10^{-3}$. However, the Basilisk simulation becomes unstable closer to pinch-off, whereas JAM successfully reaches $R_{min}/R_0 = 10^{-5}$.

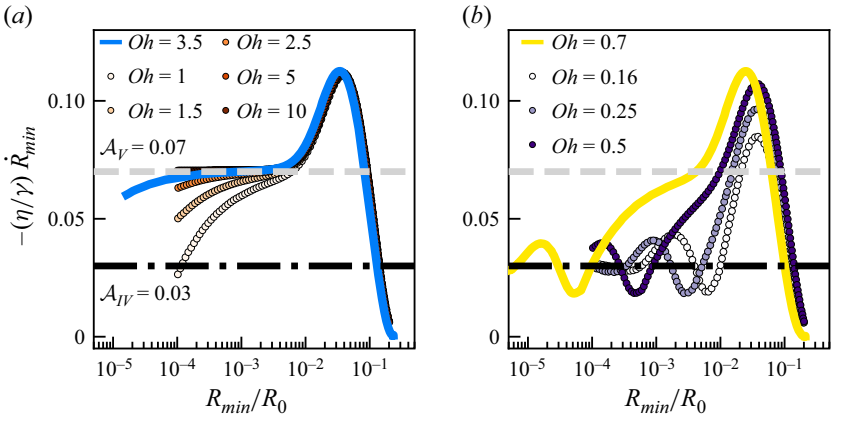

Figure 7. Validation of our numerical methods. Comparison of our numerical results (solid lines) with the numerical results of Li & Sprittles (2016) in the same geometry (dots) – (*a*) viscous regime and (*b*) visco-inertial regime.

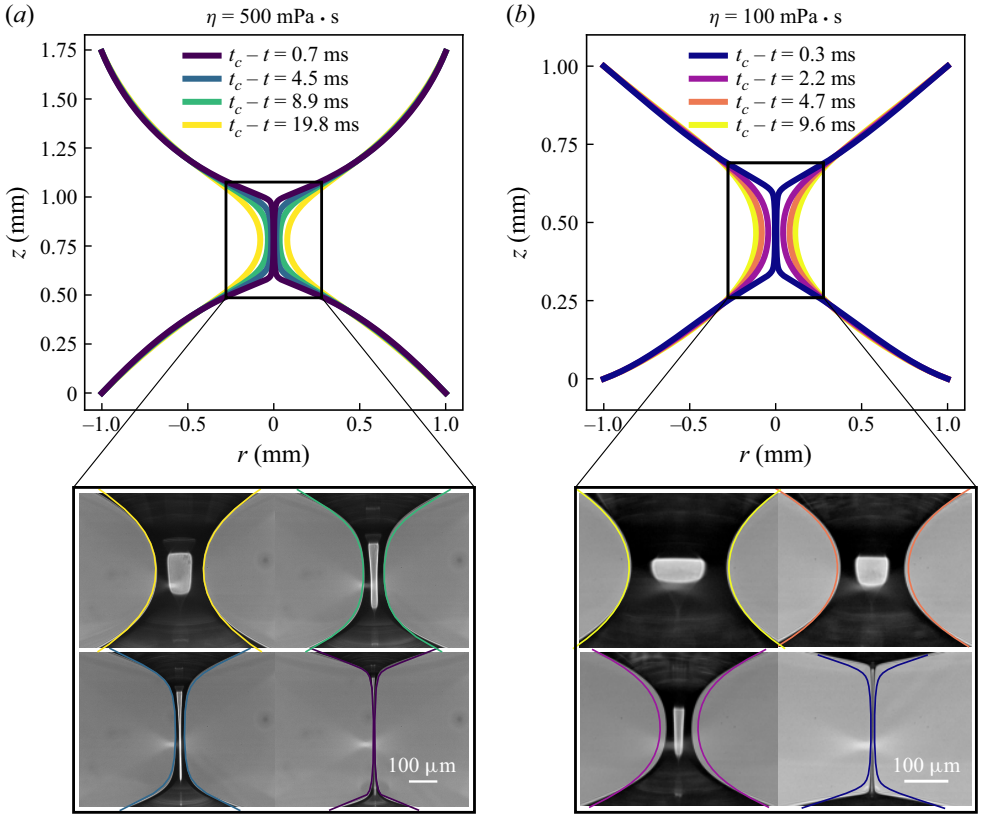

Figure 8. Full numerical profiles – $R_0 = 1$ mm, (*a*) $\eta = 500$ mPa · s and (*b*) $\eta = 100$ mPa · s. Top, complete numerical profiles and bottom, direct comparison between experimental and numerical profiles on the same scale.

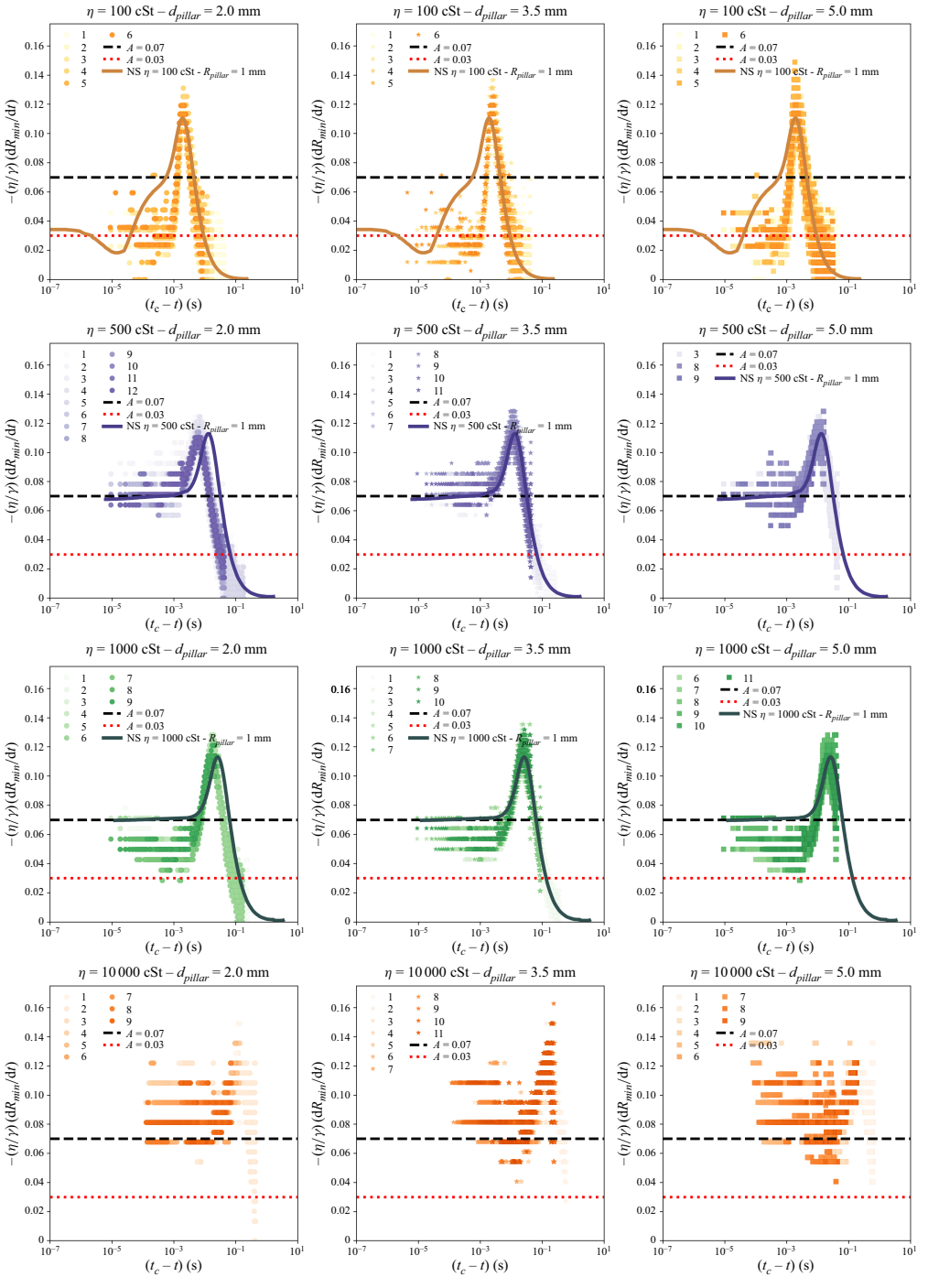

Figure 9. Instantaneous shrinking speed as a function of the time to pinch-off for different viscosities (increasing from top to bottom) and for different values of the plate radius R_0 (increasing from left to right). Experimental data are obtained from different consecutive runs, from which the average values are computed. Error bars represent the dispersion of the data, as shown in figures 2 and 3.

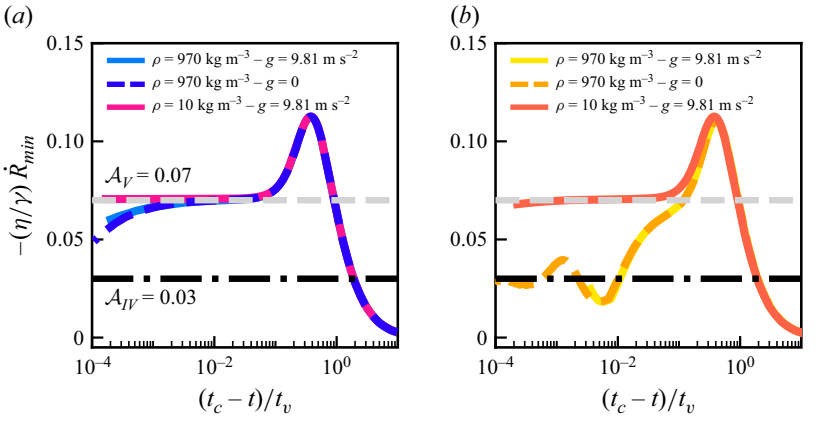

Figure 10. Effect of gravity and inertia on the dimensionless instantaneous shrinking speed $-\eta/\gamma\,\dot{R}_{min}$. In both cases, $R_0 = 1$ mm (*a*) $\eta = 500$ mPa · s, $Oh = 3.5$ (*b*) $\eta = 100$ mPa · s, $Oh = 0.7$.

At $R_{min}/R_0 = 10^{-3}$, the interface profiles obtained from both codes are in excellent agreement (figure 6*d*), further confirming the reliability of the numerical approach.

Figure 8 presents the complete numerical profiles at different times before pinch-off. The lower part of the figure provides a direct comparison between the experimental and numerical profiles on the same scale: (*a*) for the viscous case ($\eta = 500$ mPa · s, $Oh = 3.5$) and (*b*) for the visco-inertial case ($\eta = 100$ mPa · s, $Oh = 0.7$).

For the viscous case, figure 8(*a*) shows an excellent agreement between the experimental and numerical profiles, demonstrating the accuracy and reliability of the numerical results.

In contrast, for the visco-inertial case (figure 8*b*), the agreement is very good at the beginning of the experiment. However, as the system approaches pinch-off, the thinning of the liquid filament is faster in the experiments than in the numerical simulations. This discrepancy is consistent with the observations in figure 2(*c*,*e*) and is further discussed in the main text.

Appendix C. Raw experimental data

Figure 9 presents the raw experimental data showing the instantaneous shrinking speed as a function of time to pinch-off. The data are organised by viscosity (increasing from top to bottom) and plate radius (R_0) (increasing from left to right). Each panel corresponds to a distinct combination of these parameters. The experimental curves were obtained from multiple consecutive runs under the same conditions, and no additional smoothing or averaging has been applied. This figure highlights the robustness and reproducibility of the measurements across a wide range of viscosities and initial thread radii.

Appendix D. Effect of gravity and inertia

Figure 10 presents numerical simulations illustrating the evolution of the dimensionless instantaneous shrinking speed $-\dot{R}_{min}\eta/\gamma$ as a function of dimensionless time to pinch-off, for both the viscous regime (figure 10*a*) and the visco-inertial regime (figure 10*b*). In figure 10(*a*), the solid light blue line represents the case of a silicone oil studied in the main article ($\eta = 500$ mPa · s), as shown in figures 2(*b*,*d*) and 4(*a*,*c*). The dashed blue curve corresponds to the same system without gravity ($g = 0$), and the pink solid curve represents the system with gravity but no inertia ($\rho = 10$ kg/m^3). This figure demonstrates that gravity does not affect the evolution or convergence of the prefactor, while the deviation from the viscous regime value ($\mathcal{A}_V = 0.07$) near pinch-off is attributed to inertia,

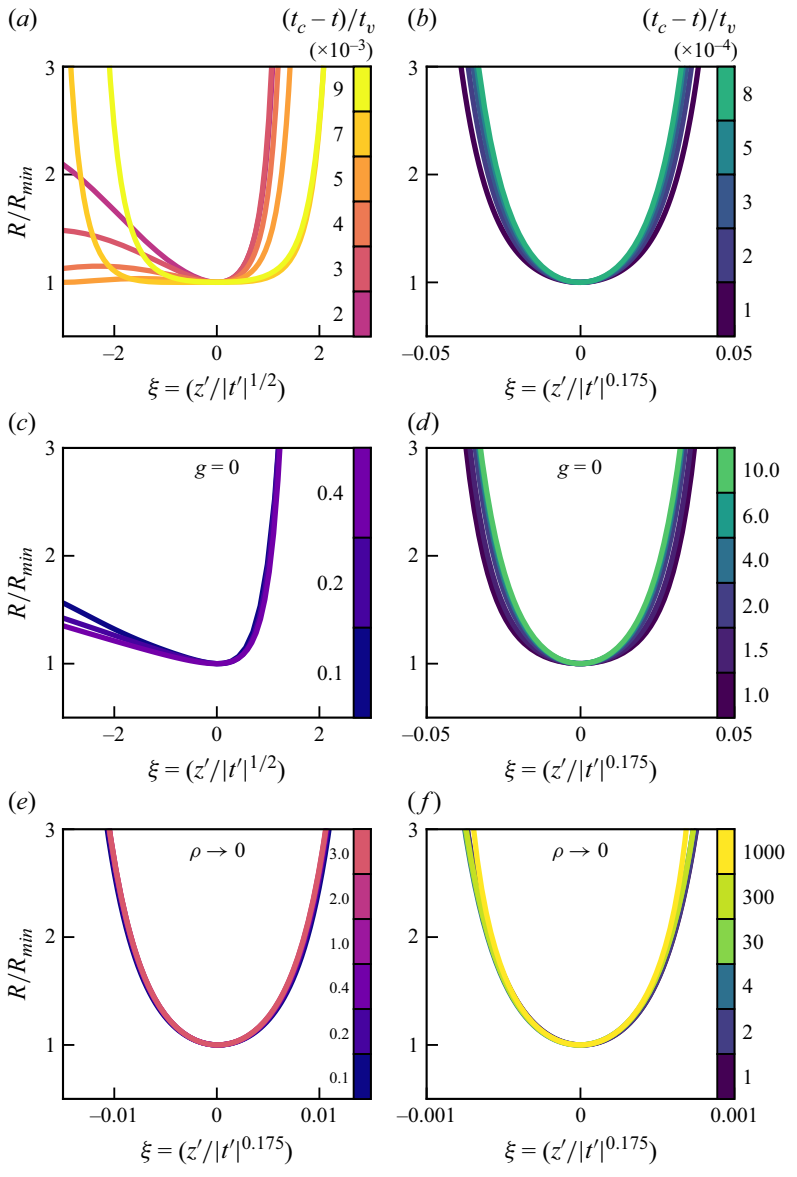

Figure 11. Effect of gravity and inertia on the profiles. In all cases $R_0 = 1$ mm, left column $\eta = 100$ mPa · s and right column $\eta = 500$ mPa · s. Panels show (*a*,*b*) $\rho = 970$ kg m^{-3}, $g = 9.81$ m s^{-2}, (*c*,*d*) $\rho = 970$ kg m^{-3}, $g = 0$ and (*e*,*f*) $\rho = 10$ kg m^{-3}, $g = 9.81$ m s^{-2}.

as it is absent in the case without inertia. This is further confirmed by the profile analysis in figures 11(*b*,*d*), and 11(*f*), where profiles in the classical case (figure 11*b*) and the case without gravity (figure 11*d*) exhibit similar behaviours, diverging from the self-similar solution close to pinch-off due to inertia, a feature not observed in the case without inertia (figure 11*f*).

In figure 10(*b*), the solid yellow line represents the case of a silicone oil with a lower viscosity ($\eta = 100$ mPa · s), as shown in figures 2(*c*,*e*) and 4(*b*,*d*) of the main text. The dashed orange curve corresponds to the system without gravity, and the orange solid curve represents the system with gravity but no inertia. This plot shows that gravity does not

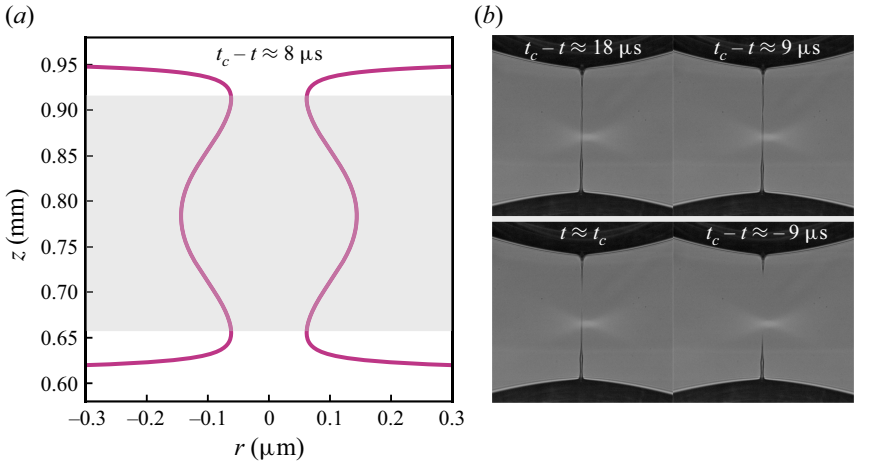

Figure 12. Liquid bridge profiles close to break-up for medium-viscosity fluid – $R_0 = 1$ mm, $\eta = 100$ mPa · s. (*a*) Numerical profile of the capillary bridge near the rupture point. The filament ruptures at two points, at the top and bottom of the shaded area. The liquid contained inside the shaded area is the future satellite drop observed after the rupture of the filament. (*b*) Images of the liquid filament before and after the pinch-off event.

impact the prefactor evolution or its oscillatory convergence. Notably, when inertia is reduced, the system converges to the viscous regime, with $\mathcal{A}_V = 0.07$. This behaviour is also evident in figure 11(*a*,*c*,*e*), where the profiles in the classical case (figure 11*a*) and without gravity (figure 11*c*) are asymmetrical and oscillates around the self-similar solution of the visco-inertial regime, preventing self-similarity. On the other hand, the profile without inertia (figure 11*e*) exhibits perfectly symmetrical profiles, indicating convergence to the viscous self-similar regime.

Appendix E. Intermediate viscosity liquid filament rupture – satellite drop

Figure 12 shows liquid bridge profiles close to the break-up point for a liquid of intermediate viscosity ($\eta = 100$ mPa · s, $R_0 = 1$ mm, $Oh = 0.7$). Figure 12(*a*) depicts the numerical liquid bridge profile in the immediate vicinity of the break-up event. The presence of a bump in the profile is indicative of the filament undergoing a rupture at two points on either side of this bump, thereby resulting in the formation of a satellite droplet once the rupture has occurred. From figure 12(*a*) we can estimate that the radius of the satellite drop is of the order of 100 nm which makes it too small to be observed experimentally. Figure 12(*b*) shows pictures of the liquid bridge before and after the pinch-off event. Here, the breakup seems to occur at a single point along the filament.

References

Ambravaneswaran, B., Phillips, S.D. & Basaran, O.A. 2000 Theoretical analysis of a dripping faucet. *Phys. Rev. Lett.* **85** (25), 5332–5335.

Ambravaneswaran, B., Subramani, H.J., Phillips, S.D. & Basaran, O.A. 2004 Dripping-jetting transitions in a dripping faucet. *Phys. Rev. Lett.* **93** (3), 034501.

Caironi, M., Gili, E., Sakanoue, T., Cheng, X. & Sirringhaus, H. 2010 High yield, single droplet electrode arrays for nanoscale printed electronics. *ACS Nano* **4** (3), 1451–1456.

Calvert, P. 2007 Printing cells. *Science* **318** (5848), 208–209.

Castrejón-Pita, Jé R., Castrejón-Pita, A.A., Thete, S.S., Sambath, K., Hutchings, I.M., Hinch, J., Lister, J.R. & Basaran, O.A. 2015 Plethora of transitions during breakup of liquid filaments. *Proc. Natl Acad. Sci.* **112** (15), 4582–4587.

CHAMPOUGNY, L., RIO, E., RESTAGNO, F. & SCHEID, B. 2017 The break-up of free films pulled out of a pure liquid bath. *J. Fluid Mech.* **811**, 499–524.
CHEN, A.U., NOTZ, P.K. & BASARAN, O.A. 2002 Computational and experimental analysis of pinch-off and scaling. *Phys. Rev. Lett.* **88** (17), 174501.
CHEN, Y.-J. & STEEN, P.H. 1997 Dynamics of inviscid capillary breakup: collapse and pinchoff of a film bridge. *J. Fluid Mech.* **341**, 245–267.
COHEN, I., BRENNER, M.P., EGGERS, J. & NAGEL, S.R. 1999 Two fluid drop snap-off problem: experiments and theory. *Phys. Rev. Lett.* **83** (6), 1147–1150.
COHEN, I. & NAGEL, S.R. 2001 Testing for scaling behavior dependence on geometrical and fluid parameters in the two fluid drop snap-off problem. *Phys. Fluids* **13** (12), 3533–3541.
DALLASTON, M.C., ZHAO, C., SPRITTLES, J.E. & EGGERS, J. 2021 Stability of similarity solutions of viscous thread pinch-off. *Phys. Rev. Fluids* **6** (10), 104004.
DAY, R.F., HINCH, E.J. & LISTER, J.R. 1998 Self-similar capillary pinchoff of an inviscid fluid. *Phys. Rev. Lett.* **80**(4), 704. publisher: APS.
DEBLAIS, A., HERRADA, M.A., HAUNER, I., VELIKOV, K.P., VAN ROON, T., KELLAY, H., EGGERS, J. & BONN, D. 2018 Viscous effects on inertial drop formation. *Phys. Rev. Lett.* **121** (25), 254501.
DOSHI, P., COHEN, I., ZHANG, W.W., SIEGEL, M., HOWELL, P., BASARAN, O.A. & NAGEL, S.R. 2003 Persistence of memory in drop breakup: the breakdown of universality. *Science* **302** (5648), 1185–1188.
EGGERS, J. 1993 Universal pinching of 3D axisymmetric free-surface flow. *Phys. Rev. Lett.* **71** (21), 3458–3460.
EGGERS, J. 1995 Theory of drop formation. *Phys. Fluids* **7** (5), 941–953.
EGGERS, J. 1997 Nonlinear dynamics and breakup of free-surface flows. *Rev. Mod. Phys.* **69** (3), 865–930.
EGGERS, J. 2012 Stability of a viscous pinching thread. *Phys. Fluids* **24** (7), 072103.
EGGERS, J. & VILLERMAUX, E. 2008 Physics of liquid jets. *Rep. Prog. Phys.* **71** (3), 036601.
GAILLARD, A., HERRADA, M.A., DEBLAIS, A., EGGERS, J. & BONN, D. 2024 Beware of caber: filament thinning rheometry does not always give 'the'relaxation time of polymer solutions. *Phys. Rev. Fluids* **9** (7), 073302.
HAUNER, I.M., DEBLAIS, A., BEATTIE, J.K., KELLAY, H. & BONN, D. 2017 The dynamic surface tension of water. *J. Phys. Chem. Lett.* **8** (7), 1599–1603.
HERRADA, M.A. & MONTANERO, J.M. 2016 A numerical method to study the dynamics of capillary fluid systems. *J. Comput. Phys.* **306**, 137–147.
KOWALEWSKI, T.A. 1996 On the separation of droplets from a liquid jet. *Fluid Dyn. Res.* **17** (3), 121–145.
LAGARDE, A., JOSSERAND, C. & PROTIÈRE, S. 2018 Oscillating path between self-similarities in liquid pinch-off. *Proc. Natl Acad. Sci.* **115** (49), 12371–12376.
LI, Y. & SPRITTLES, J.E. 2016 Capillary breakup of a liquid bridge: identifying regimes and transitions. *J. Fluid Mech.* **797**, 29–59.
PAPAGEORGIOU, D.T. 1995 On the breakup of viscous liquid threads. *Phys. Fluids* **7** (7), 1529–1544.
ROCHÉ, M., AYTOUNA, M., BONN, D. & KELLAY, H. 2009 Effect of surface tension variations on the pinch-off behavior of small fluid drops in the presence of surfactants. *Phys. Rev. Lett.* **103**, 264501.
ROTHERT, A., RICHTER, R. & REHBERG, I. 2001 Transition from symmetric to asymmetric scaling function before drop pinch-off. *Phys. Rev. Lett.* **87** (8), 084501.
RUBIO, M., PONCE-TORRES, A., VEGA, E.J., HERRADA, M.A. & MONTANERO, J.M. 2019 Complex behavior very close to the pinching of a liquid free surface. *Phys. Rev. Fluids* **4** (2), 021602.
DE SAINT VINCENT, M.R., PETIT, J., AYTOUNA, M., DELVILLE, J.P., BONN, D. & KELLAY, H. 2012 Dynamic interfacial tension effects in the rupture of liquid necks. *J. Fluid Mech.* **692**, 499–510.
SHI, X.D., BRENNER, M.P. & NAGEL, S.R. 1994 A cascade of structure in a drop falling from a faucet. *Science* **265** (5169), 219–222.
SIEROU, A. & LISTER, J.R. 2003 Self-similar solutions for viscous capillary pinch-off. *J. Fluid Mech.* **497**, 381–403.
SIRRINGHAUS, H., KAWASE, T., FRIEND, R.H., SHIMODA, T., INBASEKARAN, M., WU, W. & WOO, E.P. 2000 High-resolution inkjet printing of all-polymer transistor circuits. *Science* **290** (5499), 2123–2126.
STONE, H.A., STROOCK, A.D. & AJDARI, A. 2004 Engineering flows in small devices: microfluidics toward a lab-on-a-chip. *Annu. Rev. Fluid Mech.* **36** (1), 381–411.
XU, T., JIN, J., GREGORY, C., HICKMAN, J.J. & BOLAND, T. 2005 Inkjet printing of viable mammalian cells. *Acs. Sym. Ser.* **26** (1), 93–99.
ZHANG, W.W. & LISTER, J.R. 1999 Similarity solutions for capillary pinch-off in fluids of differing viscosity. *Phys. Rev. Lett.* **83** (6), 1151–1154.